

Visualizing Transport Structures of Time-Dependent Flow Fields

Kuangyu Shi and Hans-Peter Seidel ■ *Max-Planck Institute for Computer Science*

Holger Theisel ■ *Magdeburg University*

Tino Weinkauff and Hans-Christian Hege ■ *Zuse Institute Berlin*

This article focuses on the transport characteristics of physical properties in fluids—in particular, visualizing the finite-time transport structure of property advection. Applied to a well-chosen set of property fields, the proposed approach yields structures giving insights into the underlying flow’s dynamic processes.

Transport is an important phenomenon underlying a flow process. Any substance or property such as a dye, momentum, or heat can be transported in a fluid.¹ Modern experimental and computational fluid mechanics are increasingly concerned with transport structure. Researchers have developed many promising approaches to depict the dynamic transport behavior of flow fields. However, comprehending the important characteristics of this complex phenomenon has still proved difficult. Particularly, the nature of property transport is unclear and hard to interpret. Effective visual analysis of flow transport is still challenging.

In this article, we focus on physical properties’ transport characteristics and propose an approach to visualize the properties’ finite-time transport structures. In particular, we focus on advection, the major transport mode in a fluid. Advection involves transport of some substance or property by the macroscopic motion of currents.

The need for visual analysis

Classic approaches to dynamic-flow analysis tend to extract the transport features in Eulerian perspective and track them over time (see the “Related Work on Fluid Transport Behavior” sidebar on page 26 for more on such approaches). Although these approaches generate promising results, the extracted

features depend strongly on each instant time step and aren’t natural for dynamic analysis.

An alternative approach is Lagrangian coherent structures (LCSs), which identify the transport barriers during flow advection.² LCSs provide more natural insight into the dynamic processes of fluid transport. However, this approach doesn’t consider some important physical properties. To better understand intrinsic flow transport, we need visual analysis of physical-property transport. This analysis must include both the fluid motion and corresponding physical properties.

One way to visualize fluid transport’s dynamic behavior is to integrate the history of fluid transport over a certain time interval. To do this, you can use a transport filter that convolutes a physical-property field over time and compresses this property’s relevant transport information to an investigation point. The convolution’s results reveal the transport structures.

In advection analysis, a fluid is described as a vector field.¹ In flow visualization, a standard technique for visualizing advection trajectories is *line integral convolution* (LIC).³ LIC is similar to advecting a noise texture field along flow transport trajectories and generating the motion blur of the processed texture field. This motion blur reflects the underlying substance concentration, indicating the geometrical distribution of the related trajectories.

We propose a transport filter for fluid advection—an advection filter—which is similar to applying LIC along path lines. (Path lines are the trajectories of fluid elements.) Instead of a noise texture, the advection filter convolutes a correlated physical-property field. This is similar to

investigating the physical properties along flow transport and recording these properties' advection blur. The resulting field differs from the original physical-property field in that it reflects the transport's dynamic behavior. It's also distinct from the traditional LIC result because it captures the flow field's property characteristics.

Describing advection

In fluid dynamics, transport is macroscopic, and a fluid is a continuous medium.⁴ To describe the conservative transport of the substances or properties, we can use continuity equations.⁴

Figure 1 illustrates advection. (In figures in this article, small particles represent distributions of the transported substances or properties; they aren't necessarily real particles. Also, we use temperature color coding to characterize the time information. Red, green, and blue denote the x -, y -, and z -axis; yellow denotes the time axis in the 2D time-dependent case.) For conservative property advection without additional sources, we mathematically describe the transport mechanism as

$$\frac{\partial \Phi}{\partial t} + \nabla \cdot (\Phi \mathbf{v}) = 0$$

where Φ is the investigated property and \mathbf{v} is the flow field's velocity.

For incompressible flow, where $\nabla \cdot \mathbf{v} = 0$, we simplify the advection equation as

$$\frac{\partial \Phi}{\partial t} + \mathbf{v} \cdot \nabla \Phi = 0$$

The transport filter

The partial differential equations (PDEs) in the previous section clearly reveal property transport's physical mechanism. However, the PDEs are expressed in Eulerian perspective, and their physical pictures still aren't clear. An intuitive visualization of the underlying properties' transport behaviors can help us understand the complex phenomenon. In particular, it's critically important to see the patterns concerned with the phenomenon.

However, most flow patterns are invisible to human perception. The art of flow visualization is to make these underlying patterns visible. A common way is to identify visible distribution fields related to the phenomenon and visualize the patterns through their corresponding fields. The distribution fields are normally 2D or 3D scalar fields, which we can visualize using classic visualization approaches.

Then, the problem comes down to identifying a distribution field that captures the transport be-

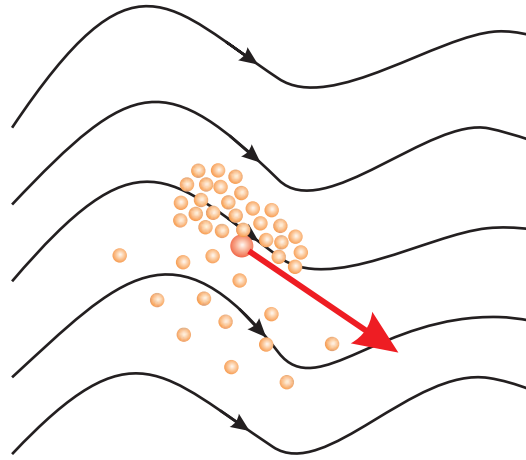


Figure 1. Advection. This transport phenomenon involves the transport of some substance or property by the macroscopic motion of currents.

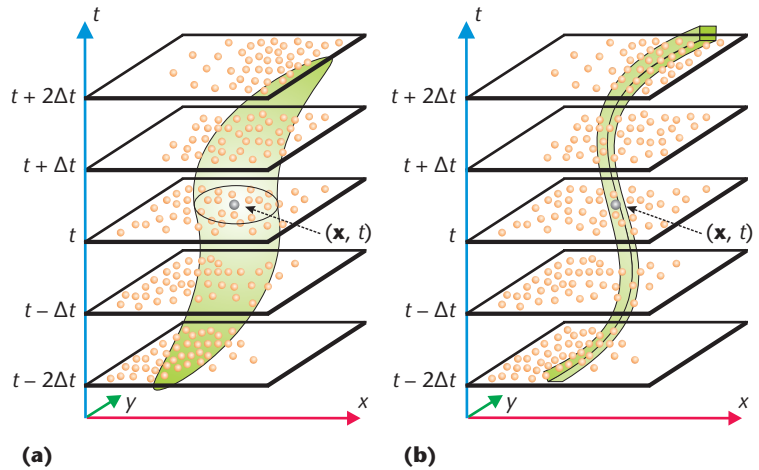


Figure 2. Transport filters for 2D unsteady-flow fields: (a) a general transport filter and (b) an advection filter. The transport filters integrate the relevant history of the underlying properties and generate the corresponding motion blur.

havior. To reflect a dynamic transport behavior, the transport process's history must be represented properly. For a given spatiotemporal investigation point, we must collect all the information relevant to transport behavior that happened at that point over a certain time interval. Convolution is powerful for identifying the relevant information in a specified domain and for increasing the visual depth into a complex phenomenon.

We use the transport filter to apply convolution in the spatiotemporal domain (see Figure 2a). The filter lets us identify the neighborhood relevant to the transport behavior and to record all the relevant information in this neighborhood. The transport filter's scale is related to the investigation's time interval and can be specified by the user.

The advection filter

Path-line LIC tracks the transport evolution over time and can effectively uncover the dynamic information of advection.⁵ It's natural to extend path-line LIC to property advection, and the advection

Related Work on Fluid Transport Behavior

Many approaches exist for exploring transport behaviors of flow fields. Traditional research tracks features such as topological features and vortex regions in Eulerian perspective¹ and typically visualizes quantity features as time-varying data sets.²

Path-line-oriented flow visualization

One standard technique for flow visualization involves path lines. Path lines are important characteristic curves in dynamic-flow fields; they describe the trajectories of flow advection. (Advection refers to the transport of some substance or property by the macroscopic motion of currents.) To formally define a path line, we start with a time-dependent vector field $\mathbf{v}(\mathbf{x}, t)$, where \mathbf{x} is the spatial component and t is the temporal component. We then define a path line $\mathbf{p}_{\mathbf{x},t}(\tau)$ starting at (\mathbf{x}, t) as

$$\mathbf{p}_{\mathbf{x},t}(\tau) = \mathbf{x} + \int_0^\tau \mathbf{v}(\mathbf{p}_{\mathbf{x},t}(\xi), t + \xi) d\xi$$

(τ is the integration time, a variable to control the length of the integration, which corresponds to the length of the corresponding path line.)

Alexander Wiebel and Gerik Scheuermann visualized a number of carefully selected path lines to get static representations of the dynamic flow.³ Holger Theisel and his colleagues considered a segmentation of the flow domain based on path lines' local properties,⁴ while Kuangyu Shi and his colleagues generated asymptotic path-line-oriented topological separation structures for periodic 2D time-dependent vector fields.⁵ Daniel Weiskopf and his colleagues applied texture-based visualization to capture path line characteristics.⁶ Kuangyu Shi and his colleagues also introduced an information visualization approach to explore the correlated structures of identified path-line attributes.⁷ Filip Sadlo and his colleagues investigated the vortex transport behavior along path lines.⁸

Line integral convolution

Another standard flow visualization technique is line integral convolution (LIC), first introduced by Brian Cabral and Leith Leedom.⁹ LIC imitates the motion blur of substance advection in a fluid, thereby describing the substance concentration due to advection.¹⁰ LIC convolutes a noisy input texture into the flow direction. This way, the resulting texture changes color only slightly in the flow direction, and rapid color changes appear perpendicular to the flow. Christof Rezk-Salama and his colleagues propose an effective extension of LIC to 3D flow visualization.¹¹ Han-Wei Shen and his colleagues use LIC to synthesize dye advection in a flow to enhance local features.¹⁰ Detlef Stalling and Hans-Christian Hege significantly improve LIC performance by exploiting

coherence along streamlines.¹² (Streamlines are those curves that are instantaneously tangent to the velocity field.) Researchers have also applied LIC with path lines to deal with unsteady flow.¹³

Lagrangian coherent structures

These structures depict the transport barriers of underlying flow processes. George Haller was the first to use a finite-time Lyapunov exponent (FTLE) field to characterize Lagrangian coherent structures (LCSs).^{14,15} He also proposed using FTLE fields' ridge lines to identify stable and unstable manifolds.¹⁶

The Lyapunov exponent of a finite-time path line is a finite-time average of the maximum expansion rate for a pair of advected particles. Consider a given point (\mathbf{x}, t) in the spatiotemporal domain and the perturbed point $\mathbf{x}' = \mathbf{x} + \delta\mathbf{x}$ of an infinitesimal perturbation $\delta\mathbf{x}$. After a time interval τ , this perturbation becomes $\delta\mathbf{x}\mathbf{p}_{\mathbf{x},t}(\tau) = \mathbf{p}_{\mathbf{x}',t}(\tau) - \mathbf{p}_{\mathbf{x},t}(\tau)$. A linear-flow map $A = \nabla\mathbf{p}_{\mathbf{x},t}(\tau)$ characterizes the perturbation's stretching gradient. The maximum stretching occurs when $\delta\mathbf{x}$ is chosen such that it's aligned with the eigenvector associated with the maximum eigenvalue of AA^T . The maximum stretching is correspondingly the largest eigenvalue of AA^T . Through logarithm computation and normalization with the absolute advection time τ , the definition of the FTLE field is

$$\delta_i^\tau = \frac{\log\left(\sqrt{\lambda_{\max}(AA^T)}\right)}{\tau}$$

Large FTLE values for forward advection correspond to unstable manifolds, whereas large FTLE values for backward advection correspond to stable manifolds. For an FTLE field $\delta_i^\tau(\mathbf{x})$, the field's ridges depict LCSs.¹⁶ Researchers have developed many algorithms to accelerate visualization of LCSs.^{17,18}

References

1. F.H. Post et al., "The State of the Art in Flow Visualisation: Feature Extraction and Tracking," *Computer Graphics Forum*, vol. 22, no. 4, 2003, pp. 775–792.
2. K.L. Ma, "Visualizing Time-Varying Volume Data," *Computing in Science & Engineering*, vol. 5, no. 2, 2003, pp. 34–42.
3. A. Wiebel and G. Scheuermann, "Eyelet Particle Tracing—Steady Visualization of Unsteady Flow," *Proc. 16th IEEE Visualization Conf. (VIS 05)*, IEEE CS Press, 2005, p. 77.
4. H. Theisel et al., "Topological Methods for 2D Time-Dependent Vector Fields Based on Stream Lines and Path Lines," *IEEE Trans. Visualization & Computer Graphics*, vol. 11, no. 4, 2005, pp. 383–394.
5. K. Shi et al., "Path-Line Oriented Topology for Periodic 2D Time-Dependent Vector Fields," *Proc. EuroVis 2006*, Eurographics Assoc., 2006, pp. 139–146.

6. D. Weiskopf et al., "Particle and Texture-Based Spatiotemporal Visualization of Time-Dependent Vector Fields," *Proc. 16th IEEE Visualization Conf. (VIS 05)*, IEEE CS Press, 2005, p. 81.
7. K. Shi et al., "Path-Line Attributes—an Information Visualization Approach to Analyzing the Dynamic Behavior of 3D Time-Dependent Flow Fields," to be published in *Proc. TopolnVis 2007*, Springer.
8. F. Sadlo, R. Peikert, and M. Sick, "Visualization Tools for Vorticity Transport Analysis in Incompressible Flow," *IEEE Trans. Visualization & Computer Graphics*, vol. 12, no. 5, 2006, pp. 949–956.
9. B. Cabral and L. Leedom, "Imaging Vector Fields Using Line Integral Convolution," *Proc. Siggraph*, ACM Press, 1993, pp. 263–270.
10. H.W. Shen, C.R. Johnson, and K.L. Ma, "Visualizing Vector Fields Using Line Integral Convolution and Dye Advection," *Proc. 1996 Symp. Volume Visualization*, ACM Press, 1996, pp. 63–70.
11. C. Rezk-Salama et al., "Interactive Exploration of Volume Line Integral Convolution Based on 3D-Texture Mapping," *Proc. 10th IEEE Visualization Conf. (VIS 99)*, IEEE CS Press, 1999, pp. 233–240.
12. D. Stalling and H.C. Hege, "Fast and Resolution-Independent Line Integral Convolution," *Proc. Siggraph*, ACM Press, 1995, pp. 249–256.
13. H.W. Shen and D. Kao, "Uflic—a Line Integral Convolution Algorithm for Visualizing Unsteady Flows," *Proc. 8th IEEE Visualization Conf. (VIS 97)*, IEEE CS Press, 1997, pp. 317–323.
14. G. Haller, "Finding Finite-Time Invariant Manifolds in Two-Dimensional Velocity Fields," *Chaos*, vol. 10, no. 1, 2000, pp. 99–108.
15. G. Haller, "Distinguished Material Surfaces and Coherent Structures in Three-Dimensional Fluid Flows," *Physica D*, vol. 149, no. 4, 2001, pp. 248–277.
16. G. Haller, "Lagrangian Coherent Structures from Approximate Velocity Data," *Physics of Fluids*, vol. 14, no. 6, 2002, pp. 1851–1861.
17. F. Sadlo and R. Peikert, "Efficient Visualization of Lagrangian Coherent Structures by Filtered AMR Ridge Extraction," *IEEE Trans. Visualization & Computer Graphics*, vol. 13, no. 6, 2007, pp. 1456–1463.
18. C. Garth et al., "Efficient Computation and Visualization of Coherent Structures in Fluid Flow Applications," *IEEE Trans. Visualization & Computer Graphics*, vol. 13, no. 6, 2007, pp. 1464–1471.

filter provides the equivalent of path-line LIC (see Figure 2b).

Given a time-dependent vector field $\mathbf{v}(\mathbf{x}, t)$, a path line $\mathbf{p}_{\mathbf{x},t}(\tau)$ starting at (\mathbf{x}, t) is a function of time. It depends on the initial position \mathbf{x} , the initial time t , and the integration time τ . Path-line integration can be carried out both forwards and backwards. In real applications, flow data is usually given in a fixed spatiotemporal domain, which means that we can integrate path lines for only a finite time. A path line starting from (\mathbf{x}, t) can also be parameterized in the form of $\mathbf{p}_{\mathbf{x},t}(s)$ with a specific arc length s .

Given a scalar property field (we discuss the specific properties we're investigating later), the advection filter calculates an intensity value I by convoluting it along path lines for either a fixed time,

$$I(\mathbf{x}, t) = \int_{T_1}^{T_2} k(\tau) \Phi(\mathbf{p}_{\mathbf{x},t}(\tau), \tau) d\tau$$

or a fixed length,

$$I(\mathbf{x}, t) = \int_{S_1}^{S_2} k(s) \Phi(\mathbf{p}_{\mathbf{x},t}(s), s) ds$$

where k denotes a filter kernel. $T_1 > 0$ and $T_2 > 0$ are the kernel lengths specifying the forward and backward integration times. The integration could be restricted to one direction simply by setting the other parameter to 0. Similarly, $S_1 > 0$ and $S_2 > 0$ specify the integration arc length in forward and backward directions.

In real applications, the resulting intensity is normalized by dividing by the total integration time (for a fixed time) or the integration arc length (for a fixed length).

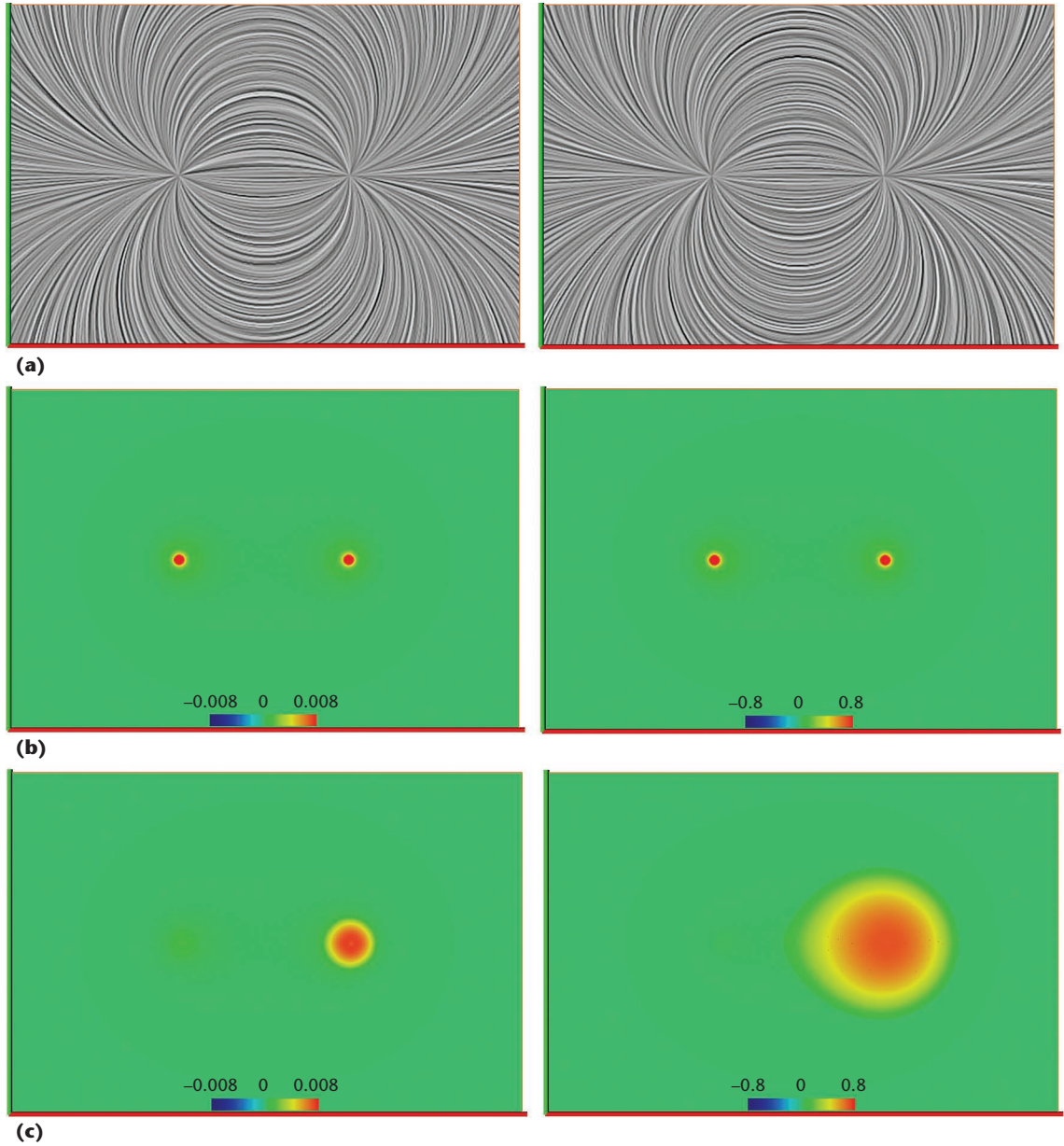
Finite-time transport structure

A simple example shows how the advection filter reveals advection structure more clearly than traditional approaches. Consider the analysis of two dipole flows of different volume flow rates per unit depth m .¹ Figure 3a (next page) compares the LIC visualizations, which display the geometrical distributions of the transport trajectories. The results are nearly the same; such visualizations aren't enough to identify the full view of a dynamic behavior.

Figure 3b shows the color coding of local kinetic energy. Structurally, the visualizations of the two dipoles are still the same. This local-property visualization doesn't fully reveal the dynamic behavior, either.

Figure 3c shows the results of using our advection filter to convolute the kinetic energy along

Figure 3. Visualization of a dipole flow, for a unit depth of $m = 0.0628$ (left column) and $m = 0.628$ (right column): (a) classic line-integral-convolution (LIC) visualization, (b) color coding of the kinetic-energy field, and (c) applying the advection filter to the kinetic-energy field. The advection filter records the dynamic information of the property transport and reveals significant different structures.



path lines and visualize the result distribution. The convoluted field's values indicate the advection magnitude; the high values correspond to the sink area. The inherent asymmetry is clear in these kinetic-energy transport structures. Analysts can distinguish the two dipoles through the difference in these structures.

For steady flow, path lines coincide with streamlines. (Streamlines are those curves that are instantaneously tangent to the velocity field.) We consider simple 2D steady flow in this section to illustrate basic ideas.

Physical properties for investigation

The general kinematic properties that we investigate here are kinetic energy, momentum, acceleration, and the local shear rate (which is a determinant of the local-shear-rate tensor).¹ For

vortex-related behaviors, we analyze properties such as vorticity, divergence, Q , and λ_2 .⁶ On the basis of our experience, no criteria to assess these properties exist.

The algorithm

We use this basic algorithm:

1. Identify the physical properties to investigate.
2. Choose a time of interest and make a sampling in the spatial domain.
3. Integrate path lines from the sampling points either forwards or backwards over a fixed time.
4. Specify a convolution kernel for the advection filter, and convolute the physical-property field along path lines.
5. Visualize the resulting convoluted field and characterize the corresponding transport structures.

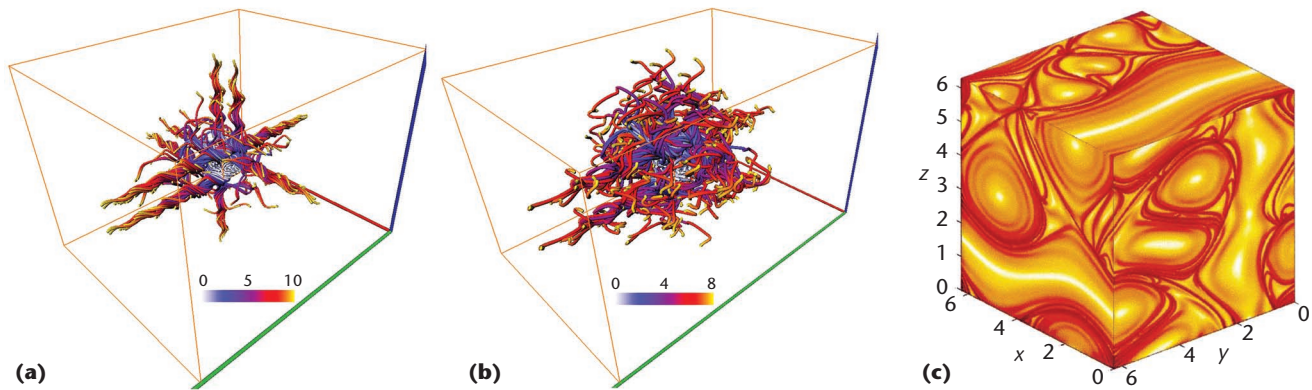


Figure 4. ABC (Arnold-Beltrami-Childress) flow: (a) path lines of steady ABC flow for integration time $T = 10$, (b) path lines of unsteady ABC flow starting at $t = 0$ for $T = 8$, and (c) the finite-time Lyapunov exponent (FTLE) field of steady ABC flow.⁶ These figures visualize the path lines used for convolution; the Lagrangian coherent structures (LCSs) revealed by the FTLE field are important transport structures that we use to compare our results. (Courtesy of George Haller, Massachusetts Inst. of Technology.)

Step 1 is the most important and flexible part of our approach. We currently select properties that have been well applied in flow analysis. However, for future applications, we could extend our approach to other properties. There are no unique criteria for selecting properties because different analyses in different applications might require different property fields. We provide users with an interface for further exploration.

In step 2, we try to make the sampling resolution as high as possible above the Nyquist rate (the minimum sampling rate to avoid aliasing for data processing). However, we must balance our computation power. During our analysis, we use an adaptive mechanism. If we find some interesting areas, we zoom in on them with a higher sampling resolution.

In step 3, we consider only finite-time path lines. We carry out path line integration in one direction within a fixed time T . We use $T > 0$ for forward integration and $T < 0$ for backward integration. Our approach has the same problem with setting the integration time that other finite-time approaches have. This problem involves a trade-off. We want to analyze path lines for as long as possible, but most of the path lines should be integrated over the same time without leaving the domain. When applying our algorithm, we carefully set the integration time. However, to the best of our knowledge, there's still no guaranteed way to optimize the setting of the integration time. We use fourth-order Runge-Kutta integration for path-line integration.

In step 4, we currently consider a simple box kernel³ and restrict the analysis to advection.

In step 5, we can choose typical scalar visualization techniques to visualize the convoluted field. Here, we apply standard direct volume rendering and color coding.

Applications

We applied our approach to data sets for ABC (Arnold-Beltrami-Childress) flow, cylinder flow, and flying jets. For each physical property we analyze, we can identify several interesting flow transport structures, which seem to hold even for different data sets.

ABC flow

We analyzed two ABC flow fields:

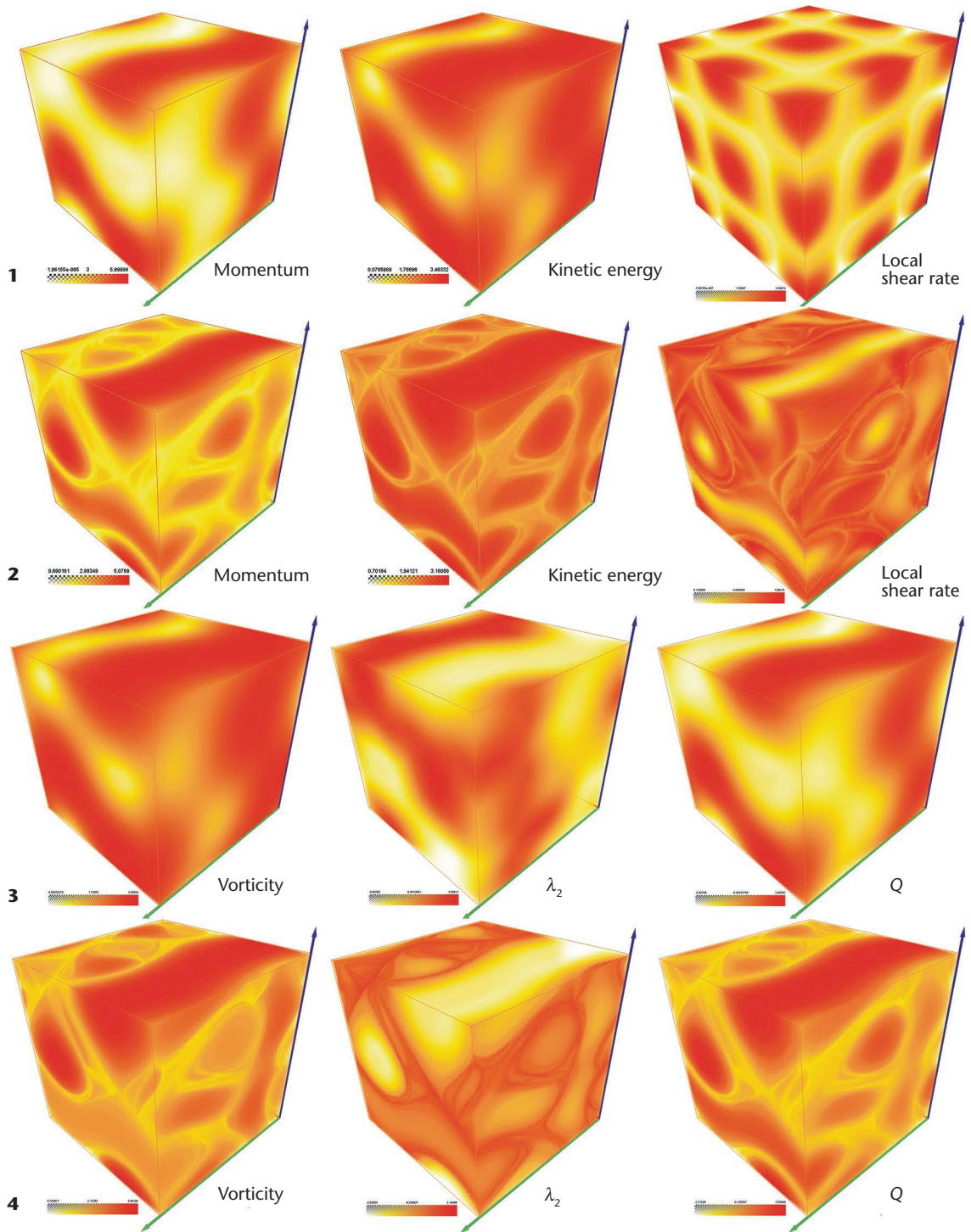
$$\mathbf{v}(\mathbf{x}, t) = \begin{pmatrix} A \sin z + B \cos y \\ B \sin x + C \cos z \\ C \sin y + A \cos x \end{pmatrix}$$

which are solutions of the Euler equation.¹ They're incompressible and inviscid. A , B , and C are three constants of the flow. Here we set $A = \sqrt{3}$, $B = \sqrt{2}$, and $C = 1$ for the steady case and $A = \sqrt{3} + 0.5t \sin(\pi t)$, $B = \sqrt{2}$, and $C = 1$ for the unsteady case. We consider the spatial domain $D = [0, 2\pi]^3$ and use a sampling of $128 \times 128 \times 128$. Because this field is also defined outside the domain, we can integrate every path line for a full time, even though it leaves the domain.

Figure 4a shows integrated path lines for the steady ABC field with integration time $T = 10$, while Figure 4b shows integrated path lines for the unsteady ABC field with $T = 8$. For comparison, Figure 4c depicts the distribution of the finite-time Lyapunov exponent (FTLE) field of the steady ABC flow.⁷ FTLE fields provide a visualization of the corresponding LCSs (for more on this, see the "Related Work on Fluid Transport Behavior" sidebar.)

Figure 5 (next page) visualizes momentum, kinetic energy, local shear rate, vorticity, Q , and λ_2 for ABC flow (Rows 1, 3, and 5) and the advection filter's corresponding results (Rows 2, 4, and 6). (In this article, T distinguishes the convoluted

Figure 5. Steady ABC flow. Rows 1 and 3 visualize the original property fields; Rows 2 and 4 visualize the advection filter's corresponding results for $T = 10$. The result of the advection filter reveals the advection behavior of the corresponding properties under the flow field.



field from the corresponding local-property field.)

In Figure 5, the first image in Rows 1 and 2 depicts the momentum field. Clearly, the advection structure in the convoluted momentum field strictly follows the corresponding LCS (depicted by the FTLE field in Figure 4c). The local maximums in the FTLE field correspond to the local minimums in the convoluted momentum field. It's reasonable that there's weak momentum advection near the LCS.

To analyze the correspondence, we make a scatter plot of these two fields (the top left of Figure 6). Al-

though simple global functions can't describe these two fields' relationships, we can still see the general inverse mapping between the fields. Furthermore, we see that this mapping is formed with several bundle structures, which might indicate local correlations.

For further analysis of these local correlations, we select areas with simple obvious patterns and observe the scatter plot of these two fields on the restricted area. Figure 7 selects an area on an x - y slice, while Figure 8 (page 32) selects an area on an x - z slice. In the upper-left scatter plot in Figure 7,

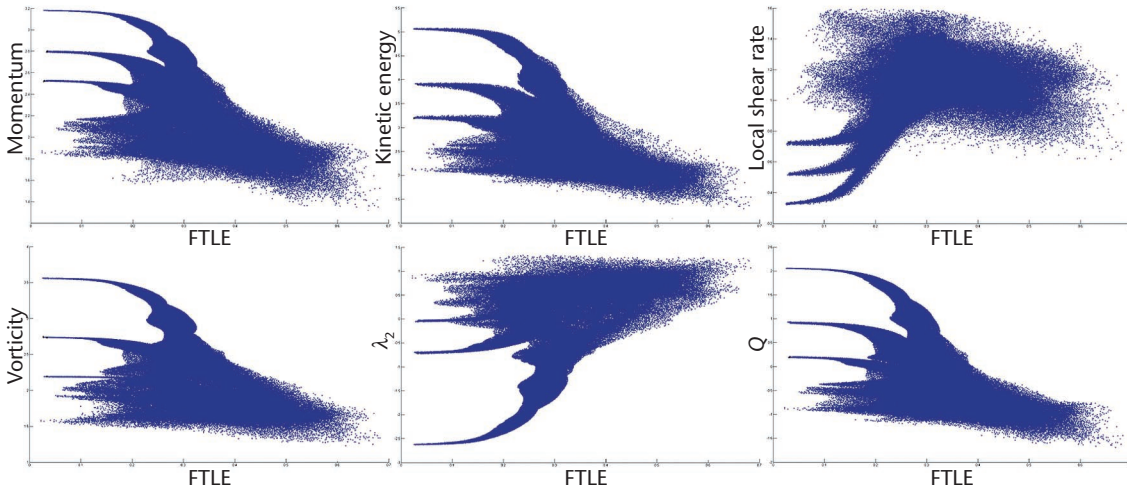


Figure 6. Steady ABC flow: scatter plots of the advection-filter-convoluted fields and corresponding FTLE fields for different physical properties. For all graphs, $T = 10$. These images show that there are special relations between the finite advection structures and the LCSs.

we see that the two fields have strong inverse correlations, although they aren't linearly related. In the upper-left scatter plot in Figure 8, we see two types of mappings, which correspond to the two types of similarities between the momentum advection structure and the corresponding LCS.

In the remaining images in Figures 5–7, we can see again similarities between the advection structures and the LCSs. Although the relationships of these similarities are different, the local correlations between the patterns are clear and agree with the vi-

sual observations between the corresponding fields.

In Figure 9, (page 33) we apply our approach to the unsteady ABC field and compare it with the corresponding classic FTLE fields. The first image in Rows 1 and 2 visualize FTLE fields computed at time $t = 0$ and $t = 8$ with $T = 8$ (forwards) and $T = -8$ (backwards). The rest of Figure 9 depicts the corresponding results of the advection filter for the investigated properties, and these distributions uncover the transport structures.

As with steady ABC flow, the transport structures for unsteady ABC flow are similar to the LCS for all

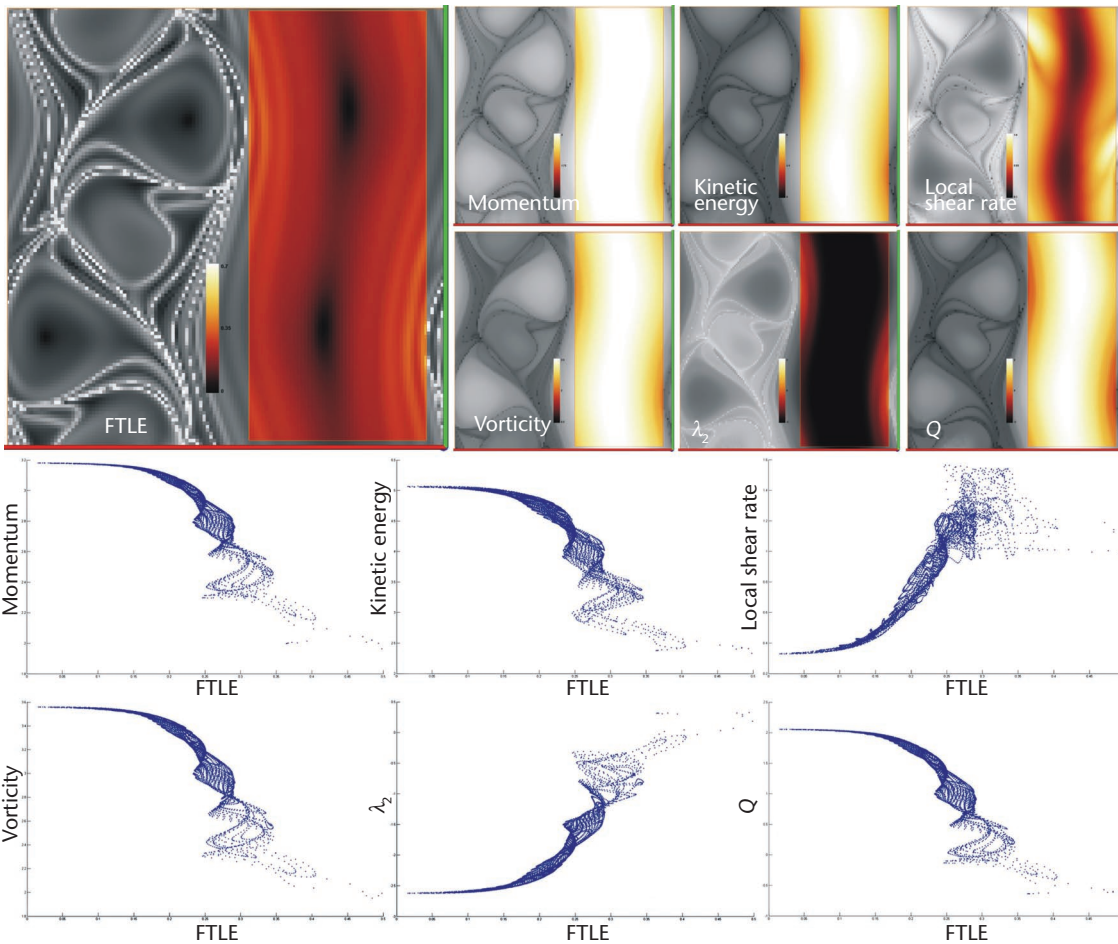
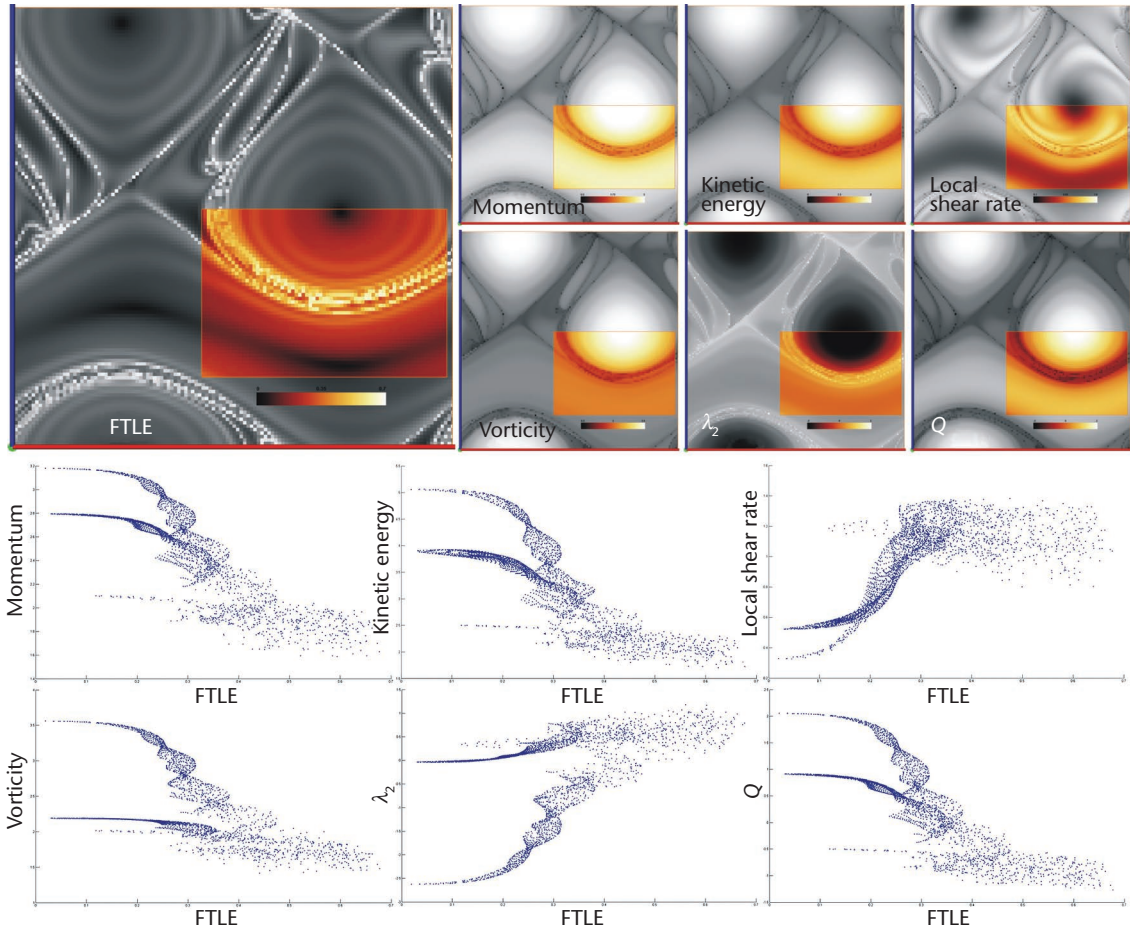


Figure 7. Steady ABC flow. The upper images visualize the fields for a selected area at slice $z = 2\pi$. The lower images visualize scatter plots of these fields and the corresponding FTLE fields. For all images, $T = 10$. Here we explore a special correspondence between these results and the LCS in a certain area with a simple pattern.

Figure 8. Steady ABC flow. The upper images visualize the fields for a selected area at slice $y = 2\pi$. The lower images visualize scatter plots of these fields and the corresponding FTLE fields. For all images, $T = 10$. Here we explore again the special correspondences between these results and the LCS in an area with another simple pattern.



the investigated properties. It's reasonable that in these cases, because the fluids are inviscid, no dissipation occurs during flow advection. So, the fluid transport is well behaved, and structurally no difference exists between material transport, momentum transport, or other property transports.

2D time-dependent cylinder flow

We also analyzed a 2D time-dependent version of the flow near a circular cylinder. The cylinder is placed at the origin, with a radius of 0.5. This is an incompressible laminar viscous flow.⁸ The data set's spatial domain is $[-9, 49.5] \times [-11, 11]$, and it involves temporal periodic flow with one period $[0, 32]$. We focus on the area behind the cylinder ($[0, 28] \times [-3.5, 3.5]$) and make a sampling of $1,000 \times 250$. For our analyses, we set $T = 5$.

Figure 10a (page 34) shows a visualization of integrated path lines starting at $t = 0$. Figure 10b shows a color coding of the corresponding FTLE field.

In Figure 11 (page 34), Rows 1, 3, and 5 depict the original local-property fields for six of the investigated properties. Rows 2, 4, and 6 depict the results of applying our advection filter along the path lines. The transport structures differ significantly from the local structures. The low values of the filtered field indicate weak flow advectations. The

advection is strong in the center area behind the cylinder but weakens as the flow moves forward. The momentum and kinetic-energy transport structures in the filtered fields are similar to the LCSs near the circular cylinder, but for the other properties, the similarity isn't so obvious. The similarity decreases when the flow travels forward.

To analyze the similarities, we pick areas with strong similarity and make the scatter plots in Figure 12 (page 35). These scatter plots reveal again the clear mapping bundles for momentum and kinetic energy.

This flow is viscous, and momentum and energy dissipation exist during transport. This means that the transport behavior of momentum and kinetic-energy advection is similar to that of material advection at the early stage. It also means that these property transport structures diffuse gradually as dissipation effects increase during flow transport. The momentum transport structures diffuse more slowly than the kinetic-energy transport structures.

Five-jet flow

Finally, we applied our approach on a 3D time-dependent flow simulating five jets flying through a domain.⁹ The data set's spatial domain is $[0, 3.81 \text{ m}]^3$ and its temporal domain is $[0, 0.06 \text{ s}]$.

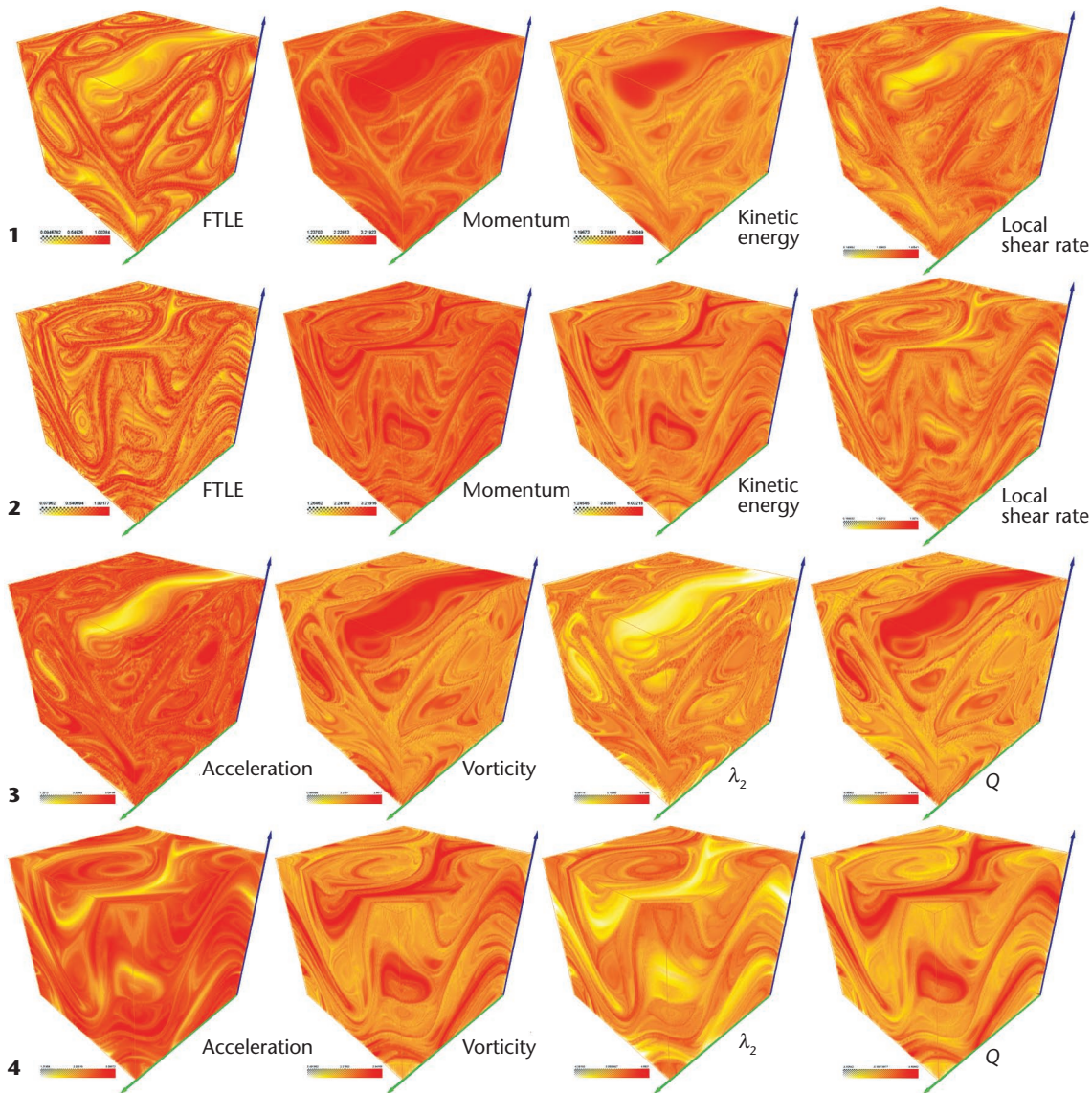


Figure 9. Unsteady ABC flow. The first image in Rows 1 and 2 visualizes the FTLE fields; the other images visualize the advection-filter-convoluted results. Rows 1 and 3 start at $t = 0$ with $T = 8$; Rows 2 and 4 start at $t = 8$ with $T = -8$. We visualize again the LCS and the advection-filter-convoluted results and see again special correspondences between these fields.

The inflow velocity is 100 m/s. This data set is compressible-flow data for which FTLE fields aren't available. We focus on the center area ($[0.8 \text{ m}, 3.01 \text{ m}]^3$), where the jets fly through, and make a sampling of $100 \times 100 \times 100$.

We performed two analyses starting at $t = 0.018 \text{ s}$ and $t = 0.024 \text{ s}$, with $T = 0.024 \text{ s}$. Figure 13 (page 36) shows the integrated path lines. In the top row in Figure 14 (page 36), we apply our approach on the density field. The left image visualizes the local density field; the middle and right images visualize the resulting fields of the advection filter for the two start times. In each resulting field, the high-value area indicates the region with strong mass advection, which describes the trend of mass concentration. The low-value area indicates the region of weak mass advection and the possible separation of mass advection.

These mass transport structures present significantly different information than the original local property fields and depend little on integration

time when it's long enough to uncover the structure. The underlying mass transport might behave asymmetrically even in a symmetric local setting.¹

In the bottom row of Figure 14, we apply our approach to the energy field. In each resulting field (the middle and right images), the high-value area indicates the energy concentration trend. The low-value area indicates weak energy advection and the possible separation of that advection. These energy transport structures are inherently asymmetric, although the local field is symmetric. They have some coherence and depend weakly on the integration time.

Unfortunately, we can't achieve accuracy in both the static and dynamic information space. The observation of dynamic transport behaviors results in the reduction of static details or even information loss. Nevertheless, this dynamic transport information provides unique views of

Figure 10. 2D dynamic cylinder flow: (a) path lines starting at $t = 0$ with $T = 5$ and (b) the corresponding FTLE field. These images visualize the path lines used for convolution; the LCSs revealed by the FTLE fields are an important transport structure that we use to compare our results.

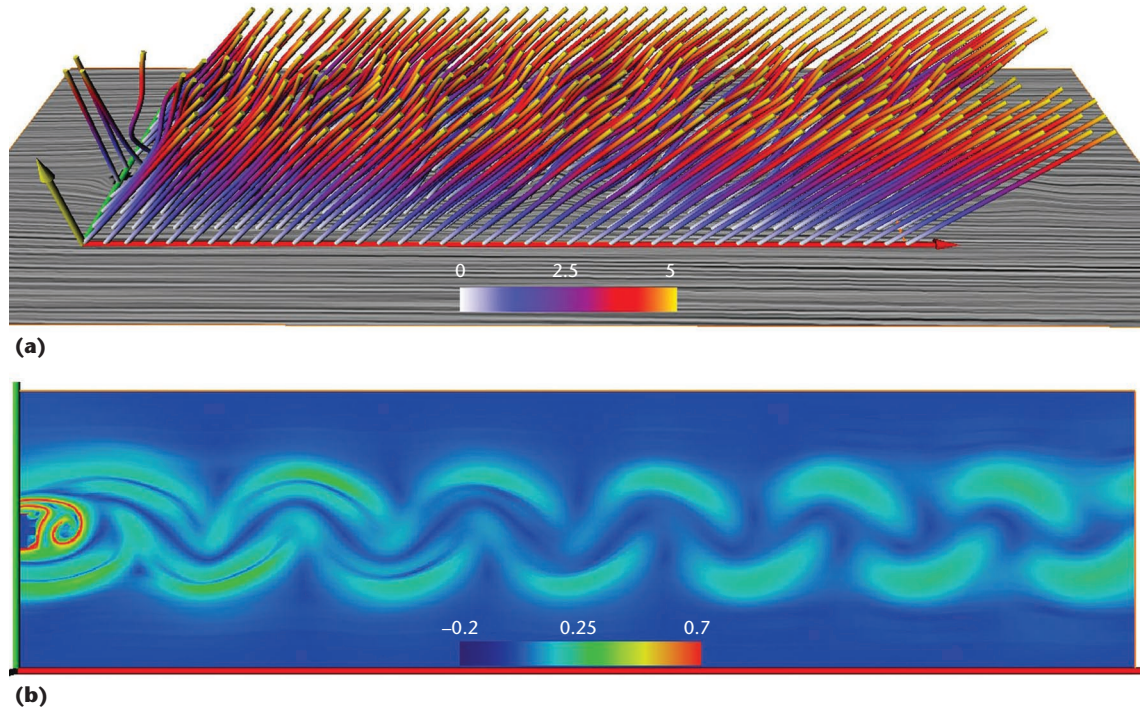
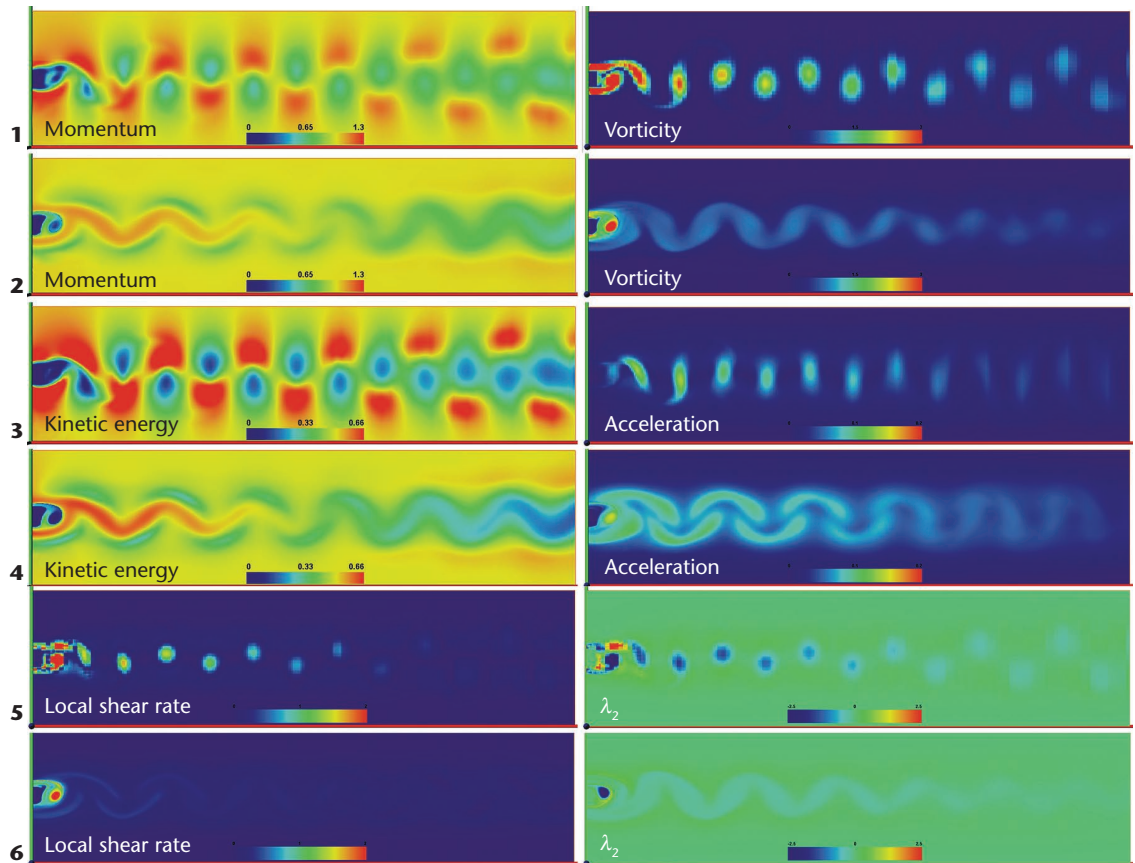


Figure 11. 2D dynamic cylinder flow. Rows 1, 3, and 5 visualize the local property fields; Rows 2, 4, and 6 visualize the corresponding advection-filter-convolution results. The result of the advection filter reveals again the advection behavior of the corresponding properties under the flow field.



transport and contributes significantly to our visual understanding of fluid dynamics. Also, we focus here only on the visual analysis of transport structures; theoretical analysis or proof is beyond this research’s scope.

For future research, we could modify the convo-

lution kernel to include other transport behaviors such as diffusion or radiation. Implementing the general transport filters directly from PDEs would also be worthwhile. Also, we could develop an algorithm that accelerates convolution, for interactive applications. 

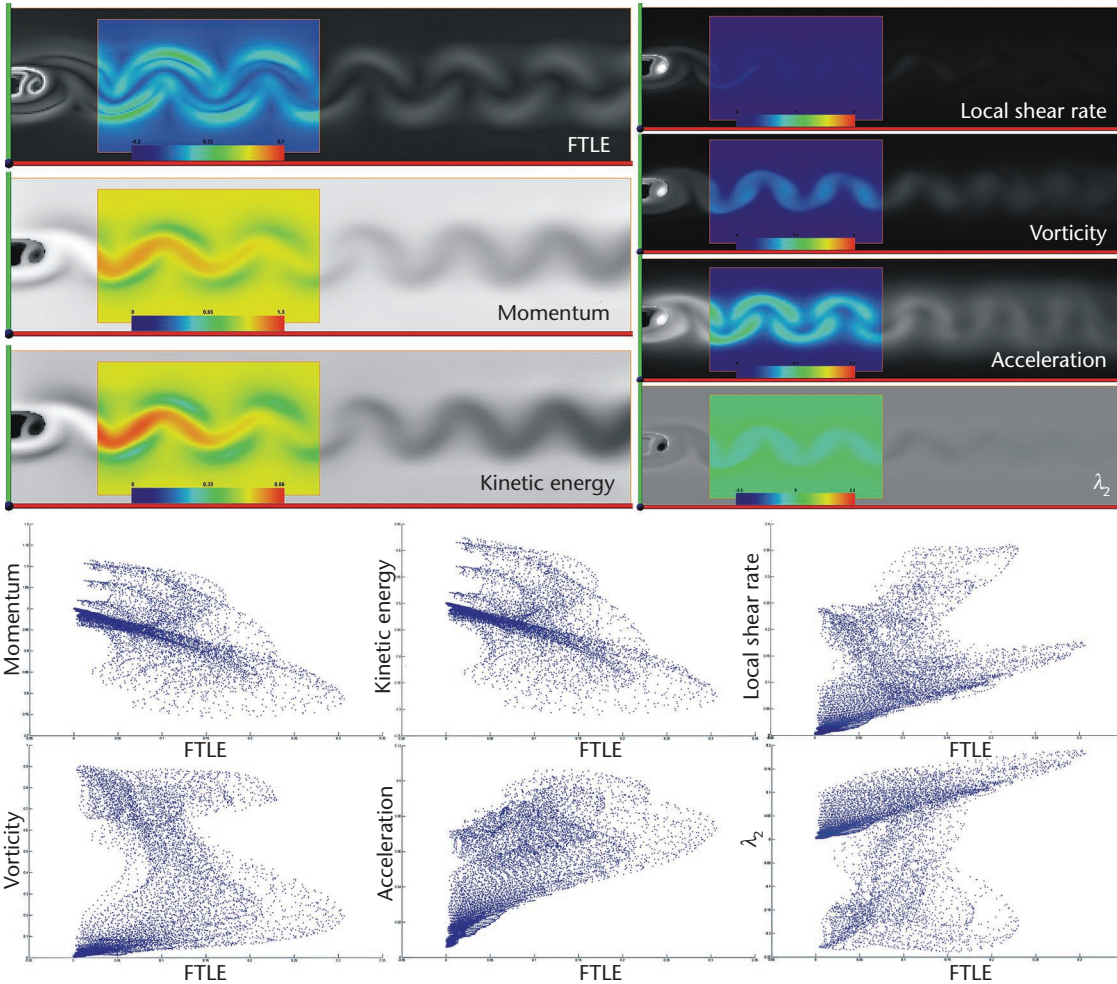


Figure 12. 2D dynamic cylinder flow. The upper images visualize the fields on a selected area of slice $t = 0$. The lower images visualize scatter plots of these fields and the corresponding FTLE fields. For all images, $T = 5$. Here we explore the correspondence between these results and the LCSs in a certain area and see relations between these fields.

Acknowledgments

We thank Gerd Mutschke (Forschungszentrum Rossendorf) and Bernd R. Noack (Technische Universität Berlin) for the cylinder flow data set. We also thank Kwan-Liu Ma and Nathan Fout (University of California, Davis) for the five-jet data set and detailed explanation. Parts of this research were funded by the Max Planck Center for Visual Computing and Communication. All visualizations in this article were created using Amira, a system for advanced visual data analysis (see <http://amira.zib.de>).¹⁰

References

1. P.K. Kundu and I.M. Cohen, *Fluid Mechanics*, Academic Press, 2004.
2. S.C. Shadden, F. Lekien, and J.E. Marsden, "Definition and Properties of Lagrangian Coherent Structures from Finite-Time Lyapunov Exponents in Two-Dimensional Aperiodic Flows," *Physica D*, vol. 212, no. 12, 2005, pp. 271-304.
3. H.W. Shen, C.R. Johnson, and K.L. Ma, "Visualizing Vector Fields Using Line Integral Convolution and Dye Advection," *Proc. Symp. Volume Visualization*, ACM Press, 1996, pp. 63-70.
4. L.G. Leal, *Advanced Transport Phenomena: Fluid Mechanics and Convective Transport Processes*, Cambridge Univ. Press, 2007.
5. H.W. Shen and D. Kao, "Uflic—a Line Integral Convolution Algorithm for Visualizing Unsteady Flows," *Proc. IEEE Visualization*, IEEE CS Press, 1997, pp. 317-323.
6. J. Jeong and F. Hussain, "On the Identification of a Vortex," *J. Fluid Mechanics*, vol. 285, Feb. 1995, pp. 69-94.
7. G. Haller, "Distinguished Material Surfaces and Coherent Structures in Three-Dimensional Fluid Flows," *Physica D*, vol. 149, no. 4, 2001, pp. 248-277.
8. H. Theisel et al., "Topological Methods for 2D Time-Dependent Vector Fields Based on Stream Lines and Path Lines," *IEEE Trans. Visualization & Computer Graphics*, vol. 11, no. 4, 2005, pp. 383-394.
9. N. Fout, K.L. Ma, and J. Ahrens, "Time-Varying Multivariate Volume Data Reduction," *Proc. ACM Symp. Applied Computing*, ACM Press, 2005, pp. 1224-1230.
10. D. Stalling, M. Westerhoff, and H.C. Hege, "Amira: A Highly Interactive System for Visual Data Analysis," *The Visualization Handbook*, Elsevier, 2005, pp. 749-767.

Kuangyu Shi is a PhD student in the Max-Planck-Institut für Informatik. His research interests include flow visualization and fluid analysis. Shi received his

Figure 13. Path lines of five-jet flow starting at (a) $t = 0.018$ s and (b) $t = 0.024$ s. The path lines visualized here are used for the convolution shown in Figure 14.

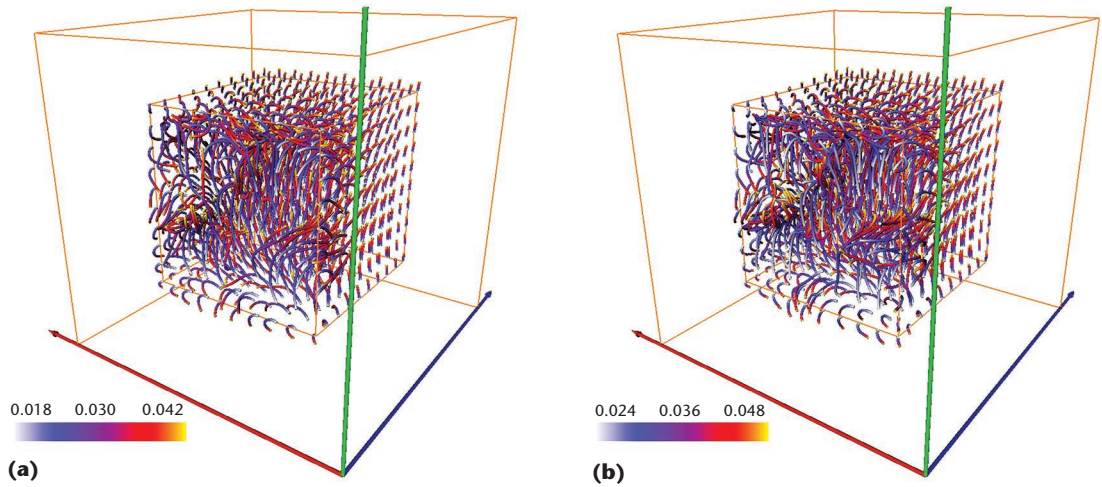
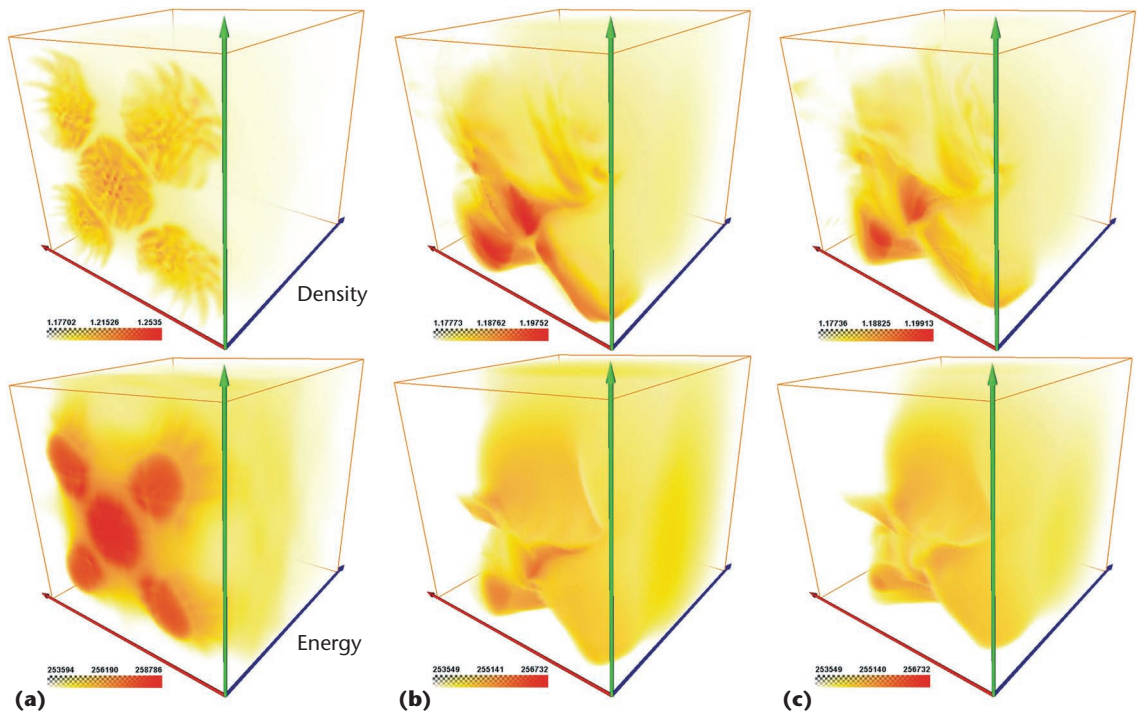


Figure 14. Five-jet flow: (a) the local density and energy fields, (b) the result of advection filter convolution starting at $t = 0.018$ s, and (c) the result of advection filter convolution starting at $t = 0.024$ s. For (b) and (c), $T = 0.024$ s. The result of the advection filter reveals again the advection behavior of the corresponding properties under the flow field, which differs significantly from the properties' corresponding static structures.



master's degree in computer science from Saarland University. Contact him at skyshi@mpi-inf.mpg.de.

Holger Theisel is a professor of visual computing at the University of Magdeburg. His research interests include flow and volume visualization as well as computer-aided geometric design, geometry processing, and information visualization. Theisel received his PhD in computer science from the University of Rostock. Contact him at theisel@isg.cs.uni-magdeburg.de.

Tino Weinkauff performs research at Zuse Institute Berlin. His research interests include flow and tensor analysis, information visualization, and geometric modeling. Weinkauff received his PhD in computer science from the University of Magdeburg. Contact him at weinkauff@zib.de.

Hans-Christian Hege is the head of Zuse Institute Berlin's Data Analysis and Visualization Department. He's interested in all aspects of data visualization and applications of visualization techniques. Hege studied physics, mathematics, and philosophy at the Free University Berlin. He's a member of the editorial boards of the Mathematics and Visualization book series and VideoMATH. Contact him at hege@zib.de.

Hans-Peter Seidel is the scientific director and chair of the computer graphics group at the Max-Planck-Institut für Informatik and a professor of computer science at Saarland University. He received his PhD in mathematics and his habilitation in computer science from Tübingen University. He was the first computer graphics researcher to receive the Leibniz Prize, in 2003. Contact him at hpseidel@mpi-inf.mpg.de.